The distinct upward curvature of the data in Fig. 3 shows that as biogenic matter containing the phosphorus and cadmium taken up from surface waters sinks down the water column and is remineralized, PO_4^{3-} is regenerated into solution sooner than Cd. Thus the regeneration cycle of Cd is deeper than that of PO_4^{3-}, as suggested earlier[2]. The degree of Cd-PO_4^{3-} curvature in these waters is much greater than that observed in other regions of the ocean, such as those used to compile the global Cd-PO_4^{3-} data in Fig. 1. This implies that in high-nutrient Antarctic and Subantarctic waters, an important fraction of Cd becomes incorporated into components of phytoplankton that are more refractory than the photosynthesized organic tissue that contains the bulk of PO_4^{3-} and other labile nutrients.

One possibility is that Cd becomes incorporated into cellular polyphosphate storage bodies which may form when surplus PO_4^{3-} is available in surface waters[12]. Alternatively, the predominance of SiO_2-secreting organisms (diatoms, radiolaria) in high-nutrient waters may lead to some incorporation of Cd into SiO_2 body parts. By contrast, warm nutrient-poor surface waters are dominated by organisms secreting $CaCO_3$. This mineral accumulates Cd in proportion to the seawater Cd/Ca ratio[2]. Per mol of PO_4^{3-}, these phytoplankton take up ~50 mol of Ca (as $CaCO_3$) and 0.03 mol of Cd[13]. As the Cd/Ca ratio in sea-water is typically less than 10^{-7}, an insignificant amount of Cd ($\sim 50 \times 10^{-7}$) is incorporated into $CaCO_3$. The bulk of Cd is presumably taken up in organic tissues in this case.

If Cd were a perfect labile nutrient analogue, the global Cd-PO_4^{3-} trend in Fig. 1 would be a straight line linking the highest Cd and PO_4^{3-} concentrations (North Pacific Deep Water) to the origin, as is the case for correlations between the two nutrients NO_3^- and PO_4^{3-} (ref. 12). In this case, waters in the region of the kink at 1.3 μmol kg^{-1} PO_4^{3-} would contain ~0.5 nmol kg^{-1} Cd. In fact, these waters contain considerably lower concentrations of Cd (~0.3 nmol kg^{-1}; Fig. 1). This reduced [Cd] could be produced by the feeding of Cd-depleted Southern Ocean waters into intermediate depths of the global ocean, provided that intermediate water input is not offset by injection of Antarctic Bottom Water (AABW), whose Cd-PO_4^{3-} properties are nearly 'normal' (Fig. 1). Estimates for the Atlantic[14] suggest a 3:1 ratio of intermediate to bottom water input. A combination of three parts Cd-depleted water having ~0.2 nmol kg^{-1} Cd with one part AABW having ~0.5 nmol kg^{-1} Cd would result in ~0.3 nmol kg^{-1} Cd, a concentration comparable to that found in the region of the kink. More detailed measurements may allow the Cd-PO_4^{3-} deviation from linearity to be used as a measure of intermediate water input from the Southern Ocean.

Clearly the influence of Cd-depleted waters has an important bearing on the use of foraminiferal Cd/Ca ratios as a circulation tracer for past oceans and as a palaeonutrient indicator. Circulation studies at intermediate water depths must take account of the Cd content of possible source waters. A single Cd-PO_4^{3-} relationship as in Fig. 1 cannot be used to deduce past nutrient levels in all oceanic regions. Specific relationships must be used in Southern ocean waters, and probably in other high-nutrient areas. Moreover, until we identify the biological mechanism responsible for Cd depletion in Southern Ocean waters, we cannot be certain that the Cd-PO_4^{3-} properties of these waters were the same in the glacial ocean. Changes in circulation or productivity, or the dominance of different phytoplankton species, could each, in principle, have altered the extent and/or geographical location of Cd depletion. □

Received 10 June; accepted 8 September 1992.

1. Shen, G. T., Boyle, E. A. & Lea, D. W. *Nature* **328,** 794–795 (1987).
2. Boyle, E. A. *Paleoceanography* **3,** 471–489 (1988).
3. Boyle, E. A. *J. geophys. Res.* **93,** 15701–15715 (1988).
4. Boyle, E. A. & Keigwin, L. D. *Nature* **330,** 35–40 (1987).
5. Boyle, E. A. *Geochim. cosmochim. Acta* **50,** 265–576 (1986).
6. Broecker, W. S. & Peng, T.-H. *Global biogeochem. Cycles* **3,** 215–239 (1989).
7. Tchernia, P. *Descriptive Regional Oceanography*, 43–45 (Pergamon, Oxford, 1980).
8. Kuehnen, E. C., Alvarez, R., Paulson, P. J. & Murphy, T. J. *Analyt. Chem.* **44,** 2050–2056 (1972).
9. Danielsson, L. *Mar. Chem.* **8,** 199–215 (1980).
10. McLellan, H. J. *Elements of Physical Oceanography*, 49 (Pergamon, 1965).
11. Martin, J. H., Gordon, R. M. & Fitzwater, S. E. *Nature* **345,** 156–158 (1990).
12. Walsh, R. S. & Hunter, K. A. *Limnol. Oceanogr.* (in the press).
13. Broecker, W. S. & Peng, T.-H. *Tracers in the Sea*, 8–14 (Eldigio, New York, 1982).
14. Tchernia, P. *Descriptive Regional Oceanography*, 161 (Pergamon, Oxford, 1980).

ACKNOWLEDGEMENTS. We thank D. Mackey and E. Butler for assistance with the Franklin samples, and E. Boyle for comments on the manuscript and his Cd-PO_4^{3-} data.

Tilt and northward offset of Cordilleran batholiths resolved using igneous barometry

Jay J. Ague & Mark T. Brandon

Department of Geology and Geophysics, Yale University, PO Box 6666, New Haven, Connecticut 06511, USA

CONSIDERABLE controversy surrounds the suggestion, based on palaeomagnetic evidence, that large segments of the North American Cordillera travelled long distances parallel to the coast during the latest Cretaceous and early Tertiary periods, well after the amalgamation of exotic terranes. Discordant palaeomagnetic data from mid-Cretaceous plutonic rocks of the Peninsular Ranges batholith of coastal southern California and Baja and the Mount Stuart batholith of the Cascade Range in Washington play a pivotal role in the controversy. The discordant data were originally interpreted to reflect northward transport of ≥1,000 km relative to cratonal North America, after the batholiths cooled through their magnetic blocking temperatures[1–5]. More recently it has been argued that the discordances arise from local tilting of batholiths, rather than northward offset[6,7]. Here we present and implement new methods based on hornblende barometry[8] for determining the palaeohorizontal in granitic batholiths and correcting palaeomagnetic data for tilting. Our results indicate that the Peninsular Ranges and Mount Stuart batholiths have undergone northward offsets of ~1,000 ±450 and ~2,900 ± 700 km, respectively, and also significant tilting.

When a batholith, or any other rock mass, undergoes large-scale displacement or rotation relative to the stable interior of a continental craton, then palaeomagnetic pole locations for rocks of comparable age from the batholith and from the craton will differ. The differences in palaeomagnetic pole locations can be used to quantify post-magnetization latitudinal offset and rotation of the batholith relative to the cratonal reference frame. The palaeomagnetic poles will also be discordant, however, if the batholith has undergone post-magnetization tilting, even if no latitudinal offset or rotation has occurred. It becomes critical, therefore, to assess palaeohorizontal in palaeomagnetic studies, so that measured directions of remanent magnetism can be corrected for the effects of tilting. Interpretation of palaeomagnetic data from calc-alkaline batholiths, such as the Peninsular Ranges batholith (PRB) and the Mount Stuart batholith (MSB), shown in Fig. 1 has long been hampered by the fact that granitic rocks preserve no internal stratigraphy from which palaeohorizontal can be reliably determined.

Our new method for addressing the problem of pluton palaeohorizontal depends on estimates of magma crystallization depth. We obtain these estimates using igneous hornblende barometry[8]. Two empirical[8,9] and three experimental[10–12] studies have shown that, in the presence of the appropriate buffer assemblage, the total aluminum content of hornblende in a crystallizing granitic magma is a sensitive linear function of pressure. Although there are differences between published barometer calibrations[8–12], they all have similar slope coefficients. Our results, therefore, are largely independent of the calibration used because we are only concerned with the

TABLE 1 Sample locations and hornblende aluminium content

Batholith	Sample	x (km) (+East)	y (km) (+North)	Z_E (km)	Al^T
PRB (West)	1011-191	−43.12	99.81	0.31	1.31
	1011-195R	−22.74	86.87	0.49	1.35
	1011-196	−13.88	87.80	0.46	1.61
	1011-201	−23.27	28.19	0.12	1.09
	1011-211	4.26	32.35	0.31	1.58
	1011-212	3.88	29.57	0.31	1.61
	1011-213	3.10	25.88	0.46	1.62
	1011-214	−1.94	25.42	0.40	1.32
	1011-238R	32.64	9.70	0.73	1.90
	1011-247	13.22	6.47	0.40	1.45
	1011-249	5.44	10.17	0.21	1.47
	1011-250	0.77	10.17	0.12	1.17
	SC-69-1b	−48.23	94.60	0.24	0.88
	SC-69-36	−10.18	84.22	0.55	1.62
	SC-69-39	6.26	67.77	0.79	1.65
PRB (East)	1011-224	25.08	79.02	1.46	1.59
	1011-225	25.84	83.18	1.68	1.66
	1011-227	16.18	93.80	1.40	1.57
	1011-228	43.29	63.31	0.79	1.69
	1011-230	51.77	64.74	1.22	1.96
	1011-231	53.94	67.00	1.07	2.05
	1011-232	55.20	69.25	0.92	2.08
	1011-234	21.65	60.53	1.13	1.31
	1011-236	17.42	44.82	0.82	1.38
	1011-239	46.24	11.29	0.73	1.74
	1011-241	53.54	25.88	0.67	1.77
	1011-242	52.77	25.42	0.79	1.94
	1011-243	50.83	24.03	0.98	1.79
	1011-244	47.34	23.57	1.28	1.59
	SC-69-40	21.76	78.06	1.07	1.76
	SC-69-41	26.06	77.72	1.40	1.77
	SC-69-43A	37.54	62.90	1.46	1.82
	SC-69-46	52.30	64.66	1.16	1.98
	SC-69-47	65.02	79.42	0.07	2.25
	SC-69-153	72.74	63.00	0.00	2.23
MSB	MS-28	9.70	−13.49	1.54	0.87
	MS-37	12.11	−13.06	1.53	0.83
	MS-47	11.91	−14.42	1.89	0.86
	MS-53	22.05	−8.84	0.67	0.92
	MS-86	16.42	−15.14	2.11	0.89
	MS-94	13.84	−15.21	2.38	0.85
	MS-101B	24.26	−3.30	0.37	0.95
	MS-103	24.35	−3.24	0.37	1.00
	MS-110B	24.23	−3.26	0.37	0.89
	MS-112	−1.88	0.19	1.18	1.20
	MS-120	−2.00	1.52	1.70	0.95
	MS-131	−3.77	−2.50	1.23	1.02
	MS-134	−4.63	−2.71	1.59	1.10
	MS-140	−4.94	−2.39	1.55	0.94
	MS-147	−14.29	9.41	0.77	1.13
	MS-149	−14.26	9.14	0.82	1.16
	MS-151	−13.98	8.41	0.88	1.22
	MS-152	−13.95	8.30	0.91	1.13
	MS-156	−13.36	6.12	0.93	1.16
	MS-171	−13.07	15.34	1.04	1.26
	MS-179	−15.21	11.03	0.50	1.36
	MS-194	−9.79	11.17	0.78	1.16
	MS-199	−9.28	11.16	0.85	1.23
	WP-454	6.21	−15.58	2.13	0.87
	WP-545	6.27	−6.37	1.87	1.14
	WP-549	5.60	−8.34	2.07	0.81

For PRB and MSB, x=0 km, y=0 km at 243° E, 33° N and 239° E, 47.617° N, respectively. Z_E, sample elevation with respect to sea level. Al^T, mean total Al formula units in rims of euhedral hornblende crystals (23 oxygen basis; all Fe^{2+}) coexisting with critical assemblage required for barometry[8-12]. Setting Fe^{3+}/Fe^{2+} to zero has a negligible effect on estimated crystallization pressures (≤0.1 kbar). Sample standard deviation in Al^T is less than 0.14 for all specimens. Prefix 1011-, Sc-69-, and WP-samples from refs 14, 15 and 17, respectively.

gradient in palaeopressures, not the absolute accuracy of each pressure determination. We calculate crystallization depth from estimated pressures by assuming an average crustal density of 2.8 g cm^{-3}.

To determine the orientation of palaeohorizontal, the least-squares method is used to fit x-y sample location data and crystallization depth estimates to a planar basis function:

$$Z_{TOT} = a_0 + a_1 x + a_2 y \quad (1)$$

where Z_{TOT} is the vertical distance from present sea level to the land surface at the time of crystallization (palaeosurface), and a_i are fit parameters. The key assumption here is that the palaeosurface was on the average parallel to palaeohorizontal, an assumption that is compatible with the physiography of analogous modern batholithic provinces, such as the Andes[13]. Z_{TOT} is then related to the depth of crystallization inferred from barometry, Z_B, by

$$Z_{TOT} = Z_B/\cos\beta + Z_E \quad (2)$$

where β is the palaeosurface dip relative to present horizontal, and Z_E denotes sample elevation (Fig. 2). This nonlinear least-squares problem is solved iteratively using standard methods.

Testing the tilt and translation hypotheses requires barometric and palaeomagnetic data for the plutons and palaeomagnetic data for the cratonal reference frame. Previously published PRB barometric data[14] are augmented here with new analyses of appropriate samples from ref. 15 (Table 1). Some reconnaissance barometric results exist for the MSB[16], but we use new determinations obtained specifically for the purpose of constraining palaeohorizontal. The bulk of the MSB samples were collected by us, but several samples from Pongsapich[17] have also been studied (Table 1). Published palaeomagnetic data for the PRB and MSB are from the western and southwestern portions of the batholiths, respectively[1-3] (Table 2). Because these parts of the batholiths crystallized at relatively shallow crustal levels, they were probably fully magnetized before tilting[18]. Plutons in the western PRB crystallized mainly between 120 and 100 Myr (ref. 19), whereas the MSB has an igneous age of 93–96 Myr (refs 20, 21). The cratonal reference frame for this period is well determined from widely separated sampling sites in North America; virtual geomagnetic pole data used here are from refs 22, 23 (Table 2).

Uncertainties in our estimates of palaeohorizontal orientation, terrane displacement and terrane rotation are best analysed using non-parametric bootstrap statistical techniques[24,25], which allow us to assess fully the random errors associated with the barometric data from the pluton, and the palaeomagnetic data from the pluton and the cratonal reference. These methods entail repeated resampling of the original data sets with replacement in order to form a large number of hypothetical data sets, or 'bootstrap samples'. The means calculated from each of these bootstrap samples, referred to as 'replicates'. are then used to determine the standard error and confidence region of an estimated value[24], such as the mean dip angle of palaeohorizontal. The replicates are calculated according to the following three steps. (1) The planar regression model is used in conjunction with bootstrap resampling of residuals[24] to determine a replicate palaeohorizontal tilt by least squares. (2) The mean magnetization direction (declination and inclination) measured at each sampling site in the pluton is corrected according to this replicate palaeohorizontal tilt. These corrected palaeomagnetic directions are resampled, and a replicate palaeomagnetic pole for the pluton is computed. (3) The published virtual geomagnetic pole locations for sampling sites comprising the cratonal reference data set are resampled to derive a replicate palaeomagnetic pole for the craton. These steps are repeated ~20,000 times to construct distributions of replicate results that map out the mean palaeomagnetic pole for the tilt-corrected pluton and the cratonal reference. These two distributions are used, in turn, to estimate the observed and expected inclination, declination and

TABLE 2 Tilt, northward offset and rotation of the PRB and MSB

Batholith	Palaeohorizontal Strike/Dip (deg)	Observed Plat (deg)	Observed Dec (deg)	Expected Plat (deg)	Expected Dec (deg)	Northwards Offset (km)	Rotation (deg)
Schmidt[12] calibration of hornblende barometer							
PRB (West)	160 ± 5.5/19 ± 5.4 W	34.8 ± 3.3	342.5 ± 8.4	43.7 ± 2.1	342.2 ± 3.3	990 ± 440	0 ± 9
PRB (East)	161 ± 7.9/15 ± 3.3 W						
MSB	55 ± 38.1/8 ± 3.0 SE	32.0 ± 6.1	16.3 ± 8.4	58.1 ± 2.2	336.9 ± 4.5	2,900 ± 720	−39 ± 10
Johnson and Rutherford[10] calibration of hornblende barometer							
PRB (West)	160 ± 5.5/17 ± 4.8 W	34.7 ± 3.4	345.3 ± 7.4	43.7 ± 2.1	342.2 ± 3.3	1,000 ± 440	−3 ± 8
PRB (East)	161 ± 8.0/13 ± 2.9 W						
MSB	55 ± 39.9/7 ± 2.5 SE	31.0 ± 5.4	15.5 ± 8.2	58.1 ± 2.2	336.9 ± 4.5	3,020 ± 650	−39 ± 9

All uncertainties are 95% confidence limits. Observed Plat and Dec, tilt-corrected palaeolatitude and declination for the pluton. Expected Plat and Dec, expected palaeolatitude and declination for the pluton. Rotations are positive counterclockwise. Uncertainty estimates calculated using 20,000 bootstrap replications. The small downward bias inherent in bootstrap standard deviation estimates was removed by selecting $n-1$ observations for each bootstrap sample, where n is the number of observations in the original data set of interest[24]. The pluton palaeomagnetic data comprise 32 and 17 site-mean directions for the PRB and MSB, respectively[1-3]. Vertical geomagnetic pole locations for cratonal North America (85 sampling sites) are from the 124 Myr Monteregian Hills intrusions in Quebec, Canada[22] and the 100 Myr Magnet Cove intrusions in Arkansas, USA[23].

palaeolatitude for the pluton, from which the mean amounts of northward offset and rotation, and associated confidence limits, are computed. The observed values reflect the location and attitude of the batholith when it was magnetized, whereas the expected values are those that would be expected for the batholith if it had always been fixed to the craton. Our bootstrap methods have been tested against standard palaeomagnetic statistical methods for comparable cases where no tilt correction is required[26]. We have found that the bootstrap-estimated means and confidence intervals are in excellent agreement (within 0.1°) with those computed using standard methods.

Our palaeohorizontal determination and error analysis methods can be used with any type of geobarometric data, either from plutons or their intruded wallrocks. Inferring patterns of batholith tilting from wallrock aureole barometry, however, is subject to considerable uncertainties associated with the timing of contact metamorphism and the relative movement between magma and wallrock which occurs during intrusion.

Analysis of pluton barometric data indicates that palaeosurfaces for the PRB and MSB are not parallel to present horizontal (Fig. 1*a* and *b*; Table 2*a* and *b*). For comparison purposes, we calculate palaeohorizontal tilt using the two experimental hornblende barometer calibrations relevant for the PRB and MSB[10,12]. The two calibrations yield nearly identical results. Our barometric data reveal a major fault with 7 km of dip separation cutting through the central PRB (Fig. 1*a*). This fault correlates

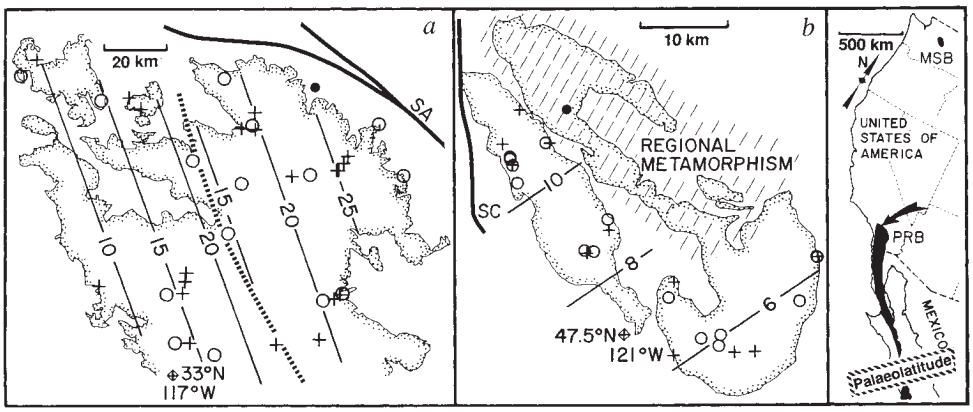

FIG. 1 Contour maps of height (Z_{TOT}; km) from present sea level to best-fit palaeosurface for the batholiths computed using hornblende barometer calibration of ref. 12 (see text and Fig. 2). +, ○, Samples having residuals above and below the best-fit surface, respectively. Average of absolute values of residuals is 1.2 km; maximum residual is 3.74 km. Location of batholiths shown in black on inset location map on right. *a*, Northern Peninsular Ranges batholith (PRB), California, USA (indicated by arrow on inset location map). SA, San Andreas fault system; ●, Palm Springs. Dashed line denotes major fault in the central part of the batholith (see text). Attitudes of best-fit palaeosurfaces to the west and east of this fault are nearly identical (Table 2). *b*, Mount Stuart batholith (MSB), Washington, USA. SC, Straight Creek fault; ●, Stevens Pass. The northeastern MSB has probably been overprinted by a regional metamorphic event[29] (dashed lines). Palaeomagnetic and barometric data used here are from the southwestern MSB. The southwestern MSB and its contact aureole show no evidence of metamorphic overprinting following intrusion. Backscattered electron imaging in the electron microprobe indicates that textures reflecting subsolidus re-equilibration of hornblende, including exsolution and 'patchy' recrystallization textures[30], are absent from all analysed MSB specimens. The excellent fit of the barometric data to the planar palaeosurface model indicates that the western and eastern PRB and southwestern MSB were tilted as coherent crustal blocks. Diagonal ruled line at bottom of location map (right) indicates approximate palaeolatitude, relative to present-day geography, of the MSB and northern PRB before northward offset (see text).

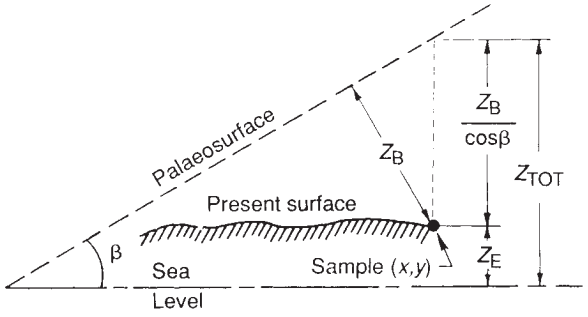

FIG. 2 Geometry of the least-squares model embodied in equation (2) of the text. View is perpendicular to the strike of the palaeosurface. For a given sample located at map coordinates (x, y), Z_B is the depth of crystallization estimated from barometry, Z_E is the sample elevation, β is the palaeosurface dip relative to present sea level, and Z_{TOT} is the vertical distance from present sea level to the palaeosurface.

with several petrologic transitions, including the well known step in oxygen isotope ratios[19,27,28]. Tilt correction of the western PRB palaeomagnetic data leads to the conclusion that the batholith has been translated northward ~1,000 ± 450 km (95% confidence) with no significant rotation since its crystallization (Fig. 1; Table 2*a* and *b*). Only about 300 km of this northward translation can be attributed to Neogene opening of the Gulf of California[7]. The MSB crystallized at shallower crustal levels than the bulk of the PRB (Fig. 1*b*). Our analysis indicates that the MSB has been translated ~2,900 ± 700 km to the north, and rotated clockwise by ~40 ± 10° since the mid-Cretaceous (Fig. 1; Table 2*a* and *b*).

Our results strongly suggest that the discordant palaeomagnetic data from the PRB and MSB are the result of tectonic tilting, northward translation, and, in the case of the MSB, clockwise rotation, following mid-Cretaceous intrusion of the batholiths. Our tilt corrections do not greatly change the large northward offsets estimated in the original palaeomagnetic studies of the batholiths, but they do lead to much smaller rotation estimates for the PRB[1,3]. It is interesting that the calculated palaeolatitudes for the PRB and MSB are indistinguishable (Fig. 1; Table 2*a* and *b*), suggesting that they originated from the same part of the Cretaceous Cordilleran magmatic arc. □

Received 27 May; accepted 5 October 1992.

1. Teissere, R. F. & Beck, M. E. Jr *Earth planet Sci. Lett.* **18,** 296–300 (1973).
2. Beck, M. E. Jr, Burmester, R. F. & Schoonover, R. *Earth planet. Sci. Lett.* **56,** 336–342 (1981).
3. Hagstrum, J. T., McWilliams, M., Howell, D. G. & Grommé, S. *Geol. Soc. Am. Bull.* **96,** 1077–1090 (1985).
4. Irving, E., Woodsworth, G. J., Wynne, P. J. & Morrison, A. *Can. J. Earth Sci.* **22,** 584–598 (1985).
5. Umhoefer, P. J. *Tectonics* **6,** 377–394 (1987).
6. Butler, R. F., Gehrels, G. E., McClelland, W. C., May, S. R. & Klepacki, D. *Geology* **17,** 691–694 (1989).
7. Butler, R. F., Dickinson, W. R. & Gehrels, G. E. *Tectonics* **10,** 561–576 (1991).
8. Hammarstrom, J. M. & Zen, E-an *Am. Miner.* **71,** 1297–1313 (1986).
9. Hollister, L. S., Grissom, G. C., Peters, E. K., Stowell, H. H. & Sisson, V. B. *Am. Miner.* **72,** 231–239 (1987).
10. Johnson, M. C. & Rutherford, M. J. *Geology* **17,** 837–841 (1989).
11. Thomas, W. M. & Ernst, W. G. in *Fluid–Mineral Interactions: A Tribute to H. P. Eugster* (Geochemical Society, 1990).
12. Schmidt, M. W. *Contrib. Miner. Petrol.* **110,** 304–310 (1992).
13. Grow, J. A. & Bowin, C. O. *J. geophys. Res.* **80,** 1449–1458 (1975).
14. Ague, J. J. & Brimhall, G. H. *Geol. Soc. Am. Bull.* **100,** 912–927 (1988).
15. Armstrong, R. L. & Suppe, J. *Geol. Soc. Am. Bull.* **84,** 1375–1392 (1973).
16. Anderson, J. L. & Paterson, S. R. *Geol. Soc. Am. Abstr. Prog.* **23,** A387 (1991).
17. Pongsapich, W. thesis, Univ. Washington (1974).
18. Beck, M. E. Jr *Tectonics* **11,** 297–302 (1992).
19. Silver, L. T., Taylor, H. P. Jr & Chappell, B. W. in *Mesozoic Crystalline Rocks-Peninsular Ranges Batholith and Pegmatites, Point Sal Ophiolite, Guidebook Geol. Soc. Am. Ann. Mtg* (1979).
20. Tabor, R. W. *et al. Geologic Map of the Chelan 30-minute by 60-minute Quadrangle, Washington* (Miscellaneous Investigations Series Map I-1661, US Geological Survey, 1987).
21. Walker, N. W. & Brown, E. H. *Geology* **19,** 714–717 (1991).
22. Foster, J. & Symmons, D. T. A. *Can J. Earth. Sci.* **16,** 1716–1725 (1979).
23. Globerman, B. R. & Irving, E. *J. geophys. Res.* **93,** 11721–11733 (1988).
24. Efron, B. *The Jacknife, the Bootstrap, and other Resampling Plans* (SIAM, Philadelphia, 1982).
25. Tauxe, L., Kylstra, N. & Constable, C. *J. geophys. Res.* **96,** 11, 723–740 (1991).
26. Demarest, H. H. Jr *J. geophys. Res.* **88,** 4321–4328 (1983).
27. Taylor, H. P. Jr *Trans. R. Soc. Edinb. Earth Sci.* **79,** 317–338 (1988).
28. Todd, V. R., Erskine, B. G. & Morton, D. M. in *Metamorphism and Crustal Evolution of the Western United States* (Prentice-Hall, Englewood Cliffs, 1988).
29. Evans, B. W. & Berti, J. W. *Geology* **14,** 695–698 (1986).
30. Blundy, J. D. & Holland, T. J. B. *Contrib. Miner. Petrol.* **111,** 269–272 (1992).

ACKNOWLEDGEMENTS. We thank J. L. Anderson, M. E. Beck Jr, R. F. Butler, G. E. Gehrels, E. Irving, R. B. Miller, S. R. Patterson and E-an Zen for comments and discussion, J. D. Blundy and L. Tauxe for reviews, and R. Burger, D. A. Evans and G. E. Tenzer for assistance in the field. This work was supported by the NSF.

Deep origin of mid-ocean-ridge seismic velocity anomalies

Wei-jia Su, Robert L. Woodward & Adam M. Dziewonski

Department of Earth and Planetary Sciences, Harvard University, Cambridge, Massachusetts 02138, USA

ZHANG and Tanimoto[1] have used the results of a new high-resolution three-dimensional model of shear-wave velocities in the Earth's upper mantle[2] to conclude that, whereas hotspots are underlain by low-velocity anomalies extending to ~200 km depth, the corresponding anomalies under mid-ocean ridges are shallower (~100 km) in extent. Here we show that such a shallow origin for the mid-ocean-ridge anomalies is inconsistent, by a factor of 3–5, with the observed travel-time residuals for the seismic phase SS (ref. 3). A three-dimensional model describing shear velocities in the entire mantle[4], derived independently of the SS observations but based on a large set of waveforms (15,000 seismograms[5]) and differential travel-time data (8,200 measurements[6,7]), shows the velocity anomalies associated with all mid-ocean ridges as continuous features down to 300 km depth. Some of these low-velocity anomalies continue throughout the upper mantle, and may extend into the lower mantle.

Visual comparison of Zhang and Tanimoto's model[1] (ZT) with, for example, M84C (ref. 8; an early three-dimensional model of the upper mantle) reveals differences other than those implied by the nominal resolution of both models: maximum harmonic degree 36 in ZT compared with 8 in M84C. The velocity anomalies in ZT, which is defined to a depth of 500 km, are smaller just below the Moho and decrease with depth rapidly to become insignificant below 300 km depth, whereas variations of ±1.5% in M84C in the transition zone, present also in model MDLSH of Tanimoto[9], are consistent with the 'degree-2' anomaly of Masters *et al.*[10].

Clearly, both models cannot be right, and each has different geodynamic implications. Model ZT, which is further discussed in refs 11 and 12, gives an impression that the heterogeneity is concentrated within the top 200–300 km, with the model becoming radially symmetric for practical purposes at greater depths. Other studies[4–10,13–16] indicate considerable lateral heterogeneity through the upper and lower mantle, although there is general agreement that the root-mean-square (r.m.s.) heterogeneity near the surface is the highest. With models of the latter sort, tomographic modelling of geodynamic observables, in other words the geoid, topography core–mantle boundary and plate motions, has been rather successful[13,17–20]. It is important to test ZT and one of the earlier models, for example M84C, preferably with data not used in the derivation of either model.

Global observations of the cap-averaged[3] (see Fig. 1*d*) travel times of the phase SS, a downward radiated shear wave reflected once at the Earth's surface, are convenient for such tests. The path through the upper mantle, although not purely vertical, is steep. The sensitivity of the SS residuals to the structure near the surface and, say, in the transition zone is comparable, but for surface waves the sensitivity to the shallow structure can be higher by an order of magnitude. Both ZT and M84C were derived using long-period surface waves.

The great circle path in Fig. 1*a* intersects the East Pacific Rise (EPR) at roughly the same place as in Fig. 1 of ref. 1. Figure 1*b* shows the cross-section along this great circle through model ZT, Fig. 1*c* the cross-section for M84C. Despite the differences in lateral resolution and amplitudes of the anomalies, the two models are somewhat similar within the top 100 km, but then they begin to diverge. In particular, in M84C the EPR anomaly persists to 300 km, and perhaps deeper, but in ZT it is limited to the top 100 km. The amplitudes in ZT fall to the background level below 300 km.

Figure 1*d* shows that the SS anomalies predicted by model ZT are limited to ±2 s and are smaller than observations by at least a factor of 3. The anomalies predicted by M84C, except for an offset between longitudes 60° W and 0°, are of roughly the size observed, reaching +10 s at the EPR and −6 s under the Sahara. The fact that the observed residuals correlate well with the surface tectonic features means that most of the SS anomaly is accumulated at shallow depths.